Wormhole Formation During Acidizing of Calcite-Cemented Fractures in Gas-Bearing Shales

Piotr Szymczak and **Kamil Kwiatkowski,** Faculty of Physics, University of Warsaw;
Marek Jarosinskí, Polish Geological Institute; **Tomasz Kwiatkowski,** National Centre for Nuclear Research;
and **Florian Osselin,** University of Warsaw and University of Calgary

Summary

A relatively large number of calcite-cemented fractures are present in gas-bearing shale formations. During hydraulic fracturing, some of these fractures will be reactivated and may become important flow paths in the resulting stimulated fracture network. On the other hand, the presence of carbonate lamina on fracture surfaces will have a hindering effect on the transport of shale gas from the matrix toward the wellbore. We investigate numerically the effect of low-pH reactive fluids on such fractures, and show that dissolution of the cement proceeds in a highly nonuniform manner. The morphology of the emerging flow paths ("wormholes") strongly depends on the thickness of the calcite layer. For thick carbonate layers, a hierarchical, fractal pattern appears, with highly branched wormhole-like channels competing for an available flow. For thin layers, the pattern is much more diffuse, with less-pronounced wormholes that merge easily with each other. Finally, for intermediate thicknesses, we observe a strong attraction between shorter and longer wormholes, which leads to the formation of islands of carbonate lamina surrounded by the dissolved regions. We argue that the wormhole-formation processes are not only important for the increase of shale-gas recovery, but also can be used for retaining the fracture permeability, even in the absence of proppant.

Introduction

The occurrence of natural fractures in shale rocks has been reported across a number of different formations in the United States (Curtis 2002; Gale et al. 2007; Gale et al. 2014; Gasparrini et al. 2014) and worldwide (Imber et al. 2014). Depending on the geological characteristics of the formations and their burial histories, natural fractures can be either open or be cemented with a different degree of sealing, from thin calcite lamina covering fracture surfaces to the fully, or almost fully, sealed veins (Curtis 2002; Asef and Farrokhrouz 2013; Gale et al. 2014). The presence of natural fractures and their impact on hydraulic fracturing and on gas production have been the subject of numerous studies (Gale et al. 2007, 2014; Walton and McLennan 2013; Li 2014). On one hand, it has been argued that natural fractures are preferentially reactivated during hydraulic fracturing, and thus might significantly contribute to the flow paths emerging in the resulting fracture system (Zhang et al. 2009). However, this does not necessarily mean that the gas production itself is enhanced. This is because of the presence of carbonate lamina at fracture surfaces, which impedes the gas exchange between shale matrix and the fracture.

A possible solution for this issue is to treat the formation with low-pH fluids, thus triggering the dissolution of the calcite layer. Matrix acidizing and acid fracturing are among the most widely used stimulation techniques of wells in conventional reservoirs (Economides and Nolte 2000; Kalfayan 2008; Frenier and Ziauddin 2008). In shale formations, acid preflush commonly is used at a spearhead stage to clear debris that may be present in the wellbore and provide a clear pathway for fracture fluids to access the formation (Grieser et al. 2007; Morsy et al. 2013a, b). As to the impact of the acid on the shale matrix itself, the opinions differ. On one hand, it is argued that such impact is expected to be minor because calcite contained in the shale matrix is not in a continuous phase and, thus, large-scale wormhole-like structures cannot be etched (Gandossi 2013). However, the results of laboratory experiments on acidization of shale fractures (Morsy et al. 2015) show a marked increase of porosity of the shale matrix as well as the development of cracks and microfractures. In a particularly relevant study, Grieser et al. (2007) observed a significant improvement in pore connectivity after the exposure of shale cores to the 3% HCl solution. The authors have concluded that acidization has a beneficial impact on the gas extraction by means of enhancing gas diffusion through narrow-aperture fractures and the associated increase of the effective surface area for flow of gas from the shale matrix. This has led to the suggestion that acidizing also can be used at a later stage, when fractures are propped, as an enhanced gas-recovery technique.

The above-mentioned studies have concentrated on the effect of acidization on the shale matrix and the induced fractures. Here, we argue that this effect is even more dramatic in the case of natural, calcite-cemented fractures. In particular, if the fraction of such fractures in the formation is high and the probability of their opening in the course of stimulation is also high, then acidization seems to be necessary for the production to be effective.

In our studies, we concentrate on the dissolution dynamics of the carbonate cement in reactivated fractures. It is known that dissolution in fractures may lead to wormhole formation, analogously to what happens during the dissolution of a porous matrix (Hanna and Rajaram 1998; Dong et al. 1999; Cheung and Rajaram 2002; Detwiler et al. 2003; Szymczak and Ladd 2009; Garcia-Rios et al. 2015). There is a large body of literature on the dissolution of porous media, mainly in the context of acidization (Hoefner and Fogler 1988; Hung et al. 1989; Fredd and Fogler 1998a; Panga et al. 2005; Kalia and Balakotaiah 2007; McDuff et al. 2010; Liu et al. 2012, 2013; Hao et al. 2013; Maheshwari et al. 2013; Maheshwari and Balakotaiah 2013; Ghommem et al. 2015; Ott and Oedai 2015; Menke et al. 2015), but the dissolution in fractures is relatively less studied, even though it is relevant not only to reservoir stimulation (Dijk and Berkowitz 1998; Durham et al. 2001; Dijk et al. 2002; Detwiler et al. 2003; Szymczak and Ladd 2009; Detwiler 2010; Ellis et al. 2011; Deng et al. 2013; Noiriel et al. 2013; Ishibashi et al. 2013; Zhang et al. 2014) but also in the context of an assessment of the long-term leakage risk in the CO_2-sequestration protocols (Smith et al. 2013; Elkhoury et al. 2013, 2015). Last, but not least, fracture dissolution

Original SPE manuscript received for review 5 May 2017. Revised manuscript received for review 29 April 2018. Paper (SPE 191376) peer approved 2 May 2018.

is the main driving process behind the cave formation in karst systems (Dreybrodt 1990; Hanna and Rajaram 1998; Cheung and Rajaram 2002; Szymczak and Ladd 2011). All these studies show that the dissolution of rock fractures is a strongly unstable process, with spontaneous focusing of the flow in high-porosity channels (wormholes). The instability here is, in fact, stronger than the corresponding instability in the dissolving porous media (Szymczak and Ladd 2011), with much weaker stabilization caused by diffusion.

It needs to be stressed that both experimental and numerical studies of fracture dissolution have considered homogeneous soluble samples, in which aperture growth is potentially unlimited. In shales, the situation is fundamentally different, because the amount of soluble cement at a given place is finite and, thus, after a certain time, the cement fully dissolves, and the dissolution front moves farther downstream. As it turns out, a limited amount of soluble material significantly influences the dissolution patterns in fractures. Nevertheless, as we show in the present study, the dissolution front is still unstable, with an intense wormhole formation in the system. Besides serving as a means to increase the fracture-matrix transport, such a nonuniform dissolution is potentially important for retaining the fracture permeability even in the absence of proppant (Gale et al. 2014; Wu and Sharma 2015). Whereas a uniformly etched fracture may close tightly under the load of overburden once the fluid pressure is removed, the nonuniform etching will tend to maintain the permeability. The less-dissolved regions will then act as supports to keep more-dissolved regions open, especially when patterns contain looped structures with islands of undissolved lamina surrounded by the dissolved regions.

The present study is inspired by the analysis of shale cores from the Pomeranian gas-bearing shale basin in Poland. The survey of 165 m of core extracted from the formation has revealed numerous natural fractures, almost all of them cemented by a carbonate cement. The analysis of the present-day stress in the formation indicates that these fractures will become reactivated, and will constitute an important part of the resulting fracture network, alongside hydraulic fractures. As we show next, in such a case, the acidization of shale fractures is an absolute necessity, serving two purposes at once: removing the lamina and creating the carbonate islands capable of supporting the overburden stress. Even though the study is centered on the Pomeranian shales, the conclusions are more general and should be applicable to any formation in which the natural fractures are carbonate-cemented.

The paper is organized as follows. First, the natural fractured veins observed in a Pomeranian gas-bearing shale basin are described briefly. Next, we introduce a mathematical and numerical approach for reactive-flow modeling. Subsequently, we analyze the resulting dissolution patterns, and characterize them in terms of effective parameters such as sweep efficiency or bypassed area fraction.

Natural Fractures in the Pomeranian Formation

The data on natural fractures used in this study have been collected from a borehole in the Pomeranian Shale Formation in Poland. The total length of 165 m of a continuous core from this borehole has been analyzed (87 mm in diameter). We have found 124 fractures crossing the core, some examples of which are shown in **Fig. 1.** Almost all the analyzed fractures are calcite-cemented, except of individual quartz veins, not considered in this study. The aperture of the cemented fractures is in a range between 0.05 and 1 mm, and their vertical extent is up to 1 m, with the average of approximately 25 cm. On the basis of the core data, it is not possible to measure directly the horizontal extension of the fractures. However, taking into account the anisotropy of the elastic properties of the shale strata and the presence of barriers to fracture propagation caused by the shale bedding, one expects the lateral extent of the fractures to exceed several times their vertical sizes. The mean fracture surface area per unit volume varies in a range from 2.4 to 3.8 m^2/m^3 in more prospective formations. This is a relatively large fracture density from the point of view of the drainage of a shale reservoir. Natural fractures of this size and density should play an important role in shale-reservoir stimulation (Daneshy 2016). The volume of mineralization in veins takes only from 2×10^{-4} to 4×10^{-4} m^3/m^3 of the entire rock volume. A relatively small amount of calcite precipitated in veins results from a small mean vein aperture that is of the order of 0.1 mm for all the formations.

We have observed two different types of textures of calcite crystals filling the veins. In the first type, the crystals are blocky, and no well-defined median line can be discerned. In the second type, the crystals are fibrous along the sides of the fracture and blocky in the median zone at the center of the fracture space **(Fig. 2).** Both of these morphologies are consistent with the evolution of antitaxial veins, as described by Bons et al. (2012)—the median zone corresponds to the seed vein, initially filled with blocky crystals. Subsequent antitaxial growth occurs on the outer surface of this seed, with fibers epitaxially overgrowing crystals in the central median zone.

The analysis of the core reveals that approximately 80% of the cemented cracks have been reopened as a result of pressure relaxation during the core excavation. This process has much in common with the effective stress release caused by rapid pore overpressure during hydraulic fracturing. Consequently, the opened fractures observed in the core should have characteristics similar to those of the fractures reopened during hydraulic fracturing, although they lack the influence of anisotropic stress control on the failure development.

When the veins open, they crack along the weakest line, which is usually either the contact area between the shale matrix and the carbonate cement or the boundary between the fibrous zone and the median zone. The exact position of cracking depends on strength ratio between host rock and vein material as well as the angle between the vein and the bulk extension direction (Virgo et al. 2013). In the analyzed core, we have observed both kinds of splitting: approximately 70% of the fractures split in the middle, leaving the carbonate cement on both walls, whereas in 30% of the cases, the splitting leaves the lamina on one of the surfaces only. With the assumption that hydraulic fracturing induces vein splitting in a manner similar to that in core excavation, one is led to the conclusion that carbonate lamina will significantly impede the gas drainage from the tight shale matrix toward the fracture.

Importantly, the analysis of the fracture orientations with respect to the principal stresses in the formation leads to the conclusion that the natural fractures will be preferentially reopened during hydraulic fracturing. The reopening will proceed in Mode II, associated with the shear displacement along the cracks. As a result, the reactivated natural fractures are expected to constitute a large portion of the total fracture network generated as a result of hydraulic fracturing.

In summary, the most feasible scenario of the reactivation of the sealed natural fractures is the following one: Under the action of shear stresses, the carbonate lamina in mineralized fractures breaks, presumably along the median line. The two surfaces are then shifted laterally with respect to each other by the shear forces. The shift will most likely be of the order of the thickness of the lamina (i.e., $\approx$0.1 mm) or smaller.

Most of such fractures will not be supported by proppant but only by the mismatch of fracture surfaces resulting from the shear offset. Because low present-day stress difference favors the opening of pre-existing fractures rather than the creation of new hydraulic fractures (Daneshy 2016), the cracked veins should be crucial for gas production in the prospective shale formations of Pomerania. However, as shown by Manchanda et al. (2014), such unpropped fractures have a tendency to close over time, and their conductivity approaches zero. A possible way out of this difficulty is to create large-scale asperities on the fracture walls by nonuniform etching by low-pH fluids, with the less-dissolved regions acting as supports to keep more-dissolved regions open. In the next section, we investigate this possibility using the numerical simulations of the dissolution process.

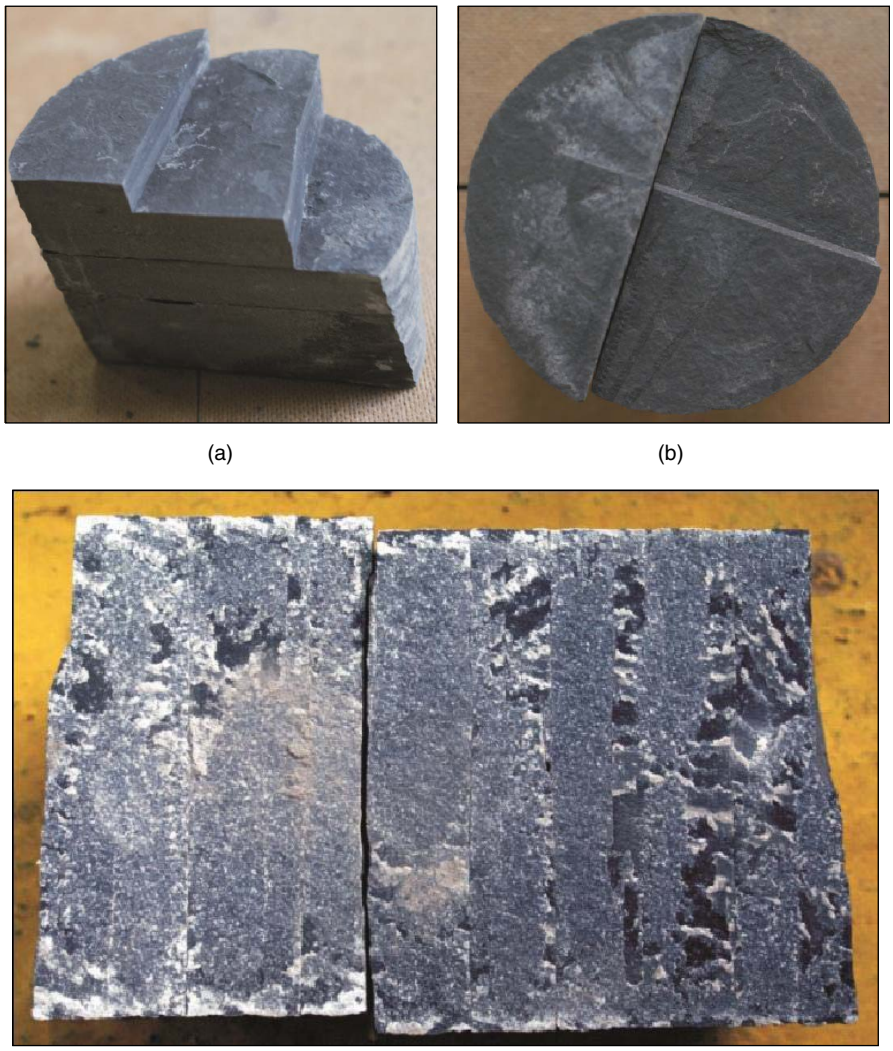

Fig. 1—(a, b) Examples of the natural fractures in the shale core from the Pomeranian gas-bearing shale basin. (c) Calcite mineralization on the sides of the open fracture. Core diameter is 87 mm.

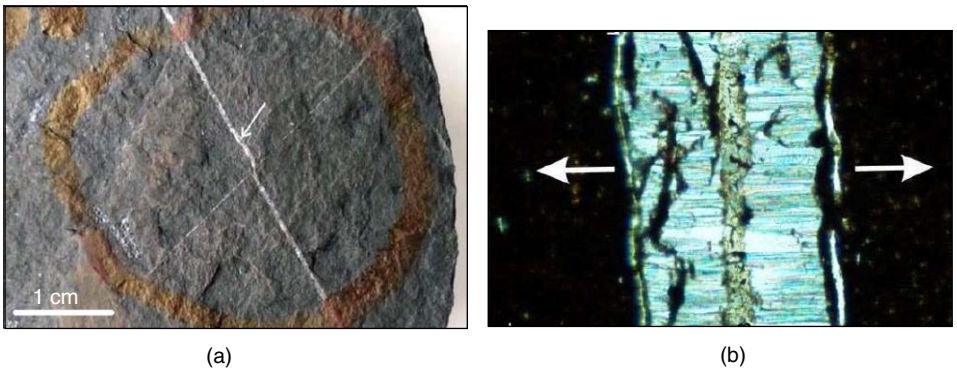

Fig. 2—(a) Two calcite-sealed fractures intersecting nearly at right angles. (b) Microscopic view of fibrous calcite filling with a blocky median zone, magnification of an area marked by an arrow in (a). Adopted from Salwa (2016).

Numerical Model

Synthetic Rock Fractures. Artificial fracture geometries used in the reactive transport simulations have been created by the following procedure, which, in its essence, follows the scenario of the reactivation of natural fractures, as described in the preceding section.

First, we create a lower surface of the crack, $S_l(x,y)$, by means of the spectral synthesis method (Saupe 1988), in which one uses a power spectral density of a fracture $g(\kappa)$ as a starting point, and then generates the spatially periodic random field with the prescribed spectral density using inverse Fourier transform. For self-affine surfaces, the spectral density obeys a power-law distribution,

$$|g(\kappa)| = A\kappa^{-(2H+2)}, \quad \ldots\ldots (1)$$

where κ is the wavenumber and H is the Hurst exponent, characterizing the self-affine geometry of rough rock surfaces. For the cracks with mineral cover in the borehole samples from the well, the Hurst exponent has been measured by Pluymakers et al. (2017) to be $H \approx 0.3$ (at micron resolution), and such a value of H is used here to create artificial fractures, with numerically generated topographies. Next, the surface $S_l(x,y)$ is replicated to form the upper surface $S_u(x,y)$, which is then translated by a distance $\delta x_t = 0.1$ mm in the tangential direction. This mimics the action of the shear forces, which are expected to reactivate the fracture. Finally, we must fix the relative position of the two fracture surfaces generated in the above manner. Naturally, as the surfaces are brought together, they come into contact and eventually begin to overlap. In a real fracture, this corresponds to the crushing of the surfaces against each other; however, in a simpler approach (Brown 1987; Oron and Berkowitz 1998; Adler and Thovert 2000), one assumes a contact (zero aperture) wherever the surfaces interpenetrate. This approximation was shown to produce acceptable results provided that the contact area stays relatively small. Walsh et al. (1997) have shown that this model correctly predicts the flow properties in fractures up to the contact areas of approximately 30%. In our case, we assume that the contact zones comprise 20% of the total fracture area.

The above procedure gives us the initial aperture field, $h_0(x,y)$, where x and y are the coordinates in the fracture plane. To fully define the system, we also must define the thicknesses of the carbonate lamina, $h_c^u(x,y)$ and $h_c^l(x,y)$, along both surfaces of the fracture. In principle, these could have been sampled from the random distribution, analogously to S_l and S_u. However, for the sake of simplicity, we will keep them constant and equal to each other: $h_c^u = h_c^l = h_c$. We have performed a number of test runs with variable h_c, finding no qualitative differences in the patterns.

Flow, Transport, and Dissolution Modeling. The mathematical model of calcite dissolution in a single narrow fracture comprises the fluid flow, reactant transport, and chemical reactions at the fracture walls leading to the evolution of fracture morphology.

Because the aperture of the fracture is several orders of magnitude smaller than its lateral dimensions, one can use a depth-averaged, quasi-2D model to simulate the flow field and the reactant transport (Hanna and Rajaram 1998; Cheung and Rajaram 2002). Fluid flow is then described by the Reynolds equation for the local volume flux (per unit length across the fracture), $\mathbf{q}(x,y,t) = \int_0^h \mathbf{v}(x,y,z,t)\mathrm{d}z$,

$$\mathbf{q}(x,y,t) = -\frac{h^3(x,y,t)}{12\mu}\nabla p(x,y,t), \quad \partial_t h + \nabla\cdot\mathbf{q}(x,y,t) = 0, \quad \ldots\ldots (2)$$

where h is the aperture of the fracture, p is the pressure, and μ is the fluid viscosity. The pressure is assumed to be uniform at the inlet and at the outlet of the computational domain representing a single fracture.

Next, the transport of hydrogen ions in the aqueous phase is described by the depth-averaged convection-diffusion-reaction equation,

$$\partial_t(hc) + \mathbf{q}\cdot\nabla c - \nabla\cdot(hD\cdot\nabla c) = 2R(c). \quad \ldots\ldots (3)$$

In Eq. 3, D is the diffusion coefficient and c is velocity-averaged concentration,

$$c(x,y,t) = \frac{1}{\mathbf{q}(x,y,t)}\int_0^{h(x,y,t)} |\mathbf{v}(x,y,z,t)| c_{3d}(x,y,z,t)\mathrm{d}z, \quad \ldots\ldots (4)$$

where $c_{3d}(x,y,z)$ is the 3D concentration field in the fracture space. Next, $R(c)$ is the reaction term, accounting for reactant transfer at each of the carbonate-laminated fracture surfaces.

In laboratory experiments on acidization of shale cores, a 3-wt% HCl solution has been used (Grieser et al. 2007; Morsy et al. 2013a, b) Similar concentrations (1–15 wt%) have been reported in industrial hydrofracking procedures (FracFocus 2017). In all cases, this corresponds to the pH smaller than 3.5. In this regime, the dissolution kinetics is well-approximated by a simple one-step reaction (Brantley et al. 2008):

$$\mathrm{CaCO_3} + \mathrm{H^+} \rightarrow \mathrm{Ca^{2+}} + \mathrm{HCO_3^-}. \quad \ldots\ldots (5)$$

The reaction rate of this reaction at low pH is well-approximated by the kinetic law that is linear in the concentration of the hydrogen ions at the mineral surface, c_w (Hoefner and Fogler 1988; Fredd and Fogler 1998a),

$$R(c) = kc_w, \quad \ldots\ldots (6)$$

with the intrinsic kinetic constant k.

To express the reactive current, R, in terms of average concentration, let us note that R must be balanced by the diffusive flux of $\mathrm{H^+}$ ions to the fracture,

$$R = R_{\mathrm{diff}} = -D(\nabla c)_w\cdot\mathbf{n}, \quad \ldots\ldots (7)$$

where $\mathbf{n}$ is the vector normal to the surface. Alternatively, the diffusive flux can be expressed in terms of the difference between the surface concentration, c_w, and the cup-mixing concentration, c, by using the geometry-dependent Sherwood number (Bird et al. 2001),

$$R_{\mathrm{diff}} = \frac{DSh}{2h}(c_w - c). \quad \ldots\ldots (8)$$

The Sherwood number itself depends on kh/D, but the variation is relatively small (Gupta and Balakotaiah 2001), bounded by two asymptotic limits: high reaction rates (transport limit) and low reaction rates (reaction limit). For our geometry (slot space with two

dissolving walls), these limits correspond to $Sh = 7.54$ and $Sh = 8.24$, respectively (Ebadian and Dong 1998; Szymczak and Ladd 2012). In the theoretical calculations, we approximate Sh by a constant value $Sh = 8$. By equating the reactive flux (Eq. 6) with the diffusive flux (Eq. 8), we obtain the standard relationship between c_w and c (Gupta and Balakotaiah 2001),

$$c_w = \frac{c}{1 + \frac{2kh}{DSh}}, \quad \ldots\ldots (9)$$

so that finally,

$$R(c) = k_{\text{eff}} c \theta(h_{\max} - h), \quad \ldots\ldots (10)$$

where

$$k_{\text{eff}}(h) = \frac{k}{1 + 2kh/DSh} \quad \ldots\ldots (11)$$

is an effective reaction rate that accounts for the diffusive slowdown of a reaction as the aperture increases. For $\frac{2kh}{DSh} \ll 1$, the dissolution kinetics is reaction-limited, and the concentration field is almost uniform across the aperture so that

$$k_{\text{eff}} \approx k. \quad \ldots\ldots (12)$$

However, for fast reaction rates (or large apertures), when $\frac{2kh}{DSh} \gg 1$, the dissolution becomes transport-limited with

$$k_{\text{eff}} \approx \frac{DSh}{2h}. \quad \ldots\ldots (13)$$

In Eq. 10, the term $\theta(h_{\max} - h)$ is the Heaviside step function, which guarantees that the reaction term vanishes in the region where all the cement has dissolved (which corresponds to the aperture $h_{\max} = h_0 + h_c^l + h_c^u$). In this region, Eq. 3 reduces to a convection-diffusion equation.

As mentioned above we assume that the thicknesses of both lamina are constant and equal to each other and, consequently, that the dissolution proceeds in a symmetrical manner. As a result, the aperture of the fracture h grows in accordance with

$$c_{\text{sol}} \frac{\partial h(x,y,t)}{\partial t} = 2R(c) = 2k_{\text{eff}} c \theta(h_{\max} - h), \quad \ldots\ldots (14)$$

where c_{sol} is the molar concentration of the solid phase ($c_{\text{sol}} = 2.7 \times 10^{-2}$ mol/cm^3 for $CaCO_3$).

Several dimensionless numbers characterize the dissolution process. The first is the Péclet number,

$$Pe = \frac{q_0}{D}, \quad \ldots\ldots (15)$$

which gives the relative ratio of the advective and diffusive transport. Here q_0 is an average value of the initial volume flux, as defined by Eq. 2. In our simulations, we take $Pe = 100$, which corresponds to the typical fluid flows used in the fracture acidization. The second is the Damköhler number,

$$Da = 2k\langle h_0 \rangle / q_0, \quad \ldots\ldots (16)$$

which relates the surface reaction rate to the rate of convective transport. In Eq. 16, $\langle h_0 \rangle$ is the average aperture of the initial fracture. As argued above, the regime of the dissolution (transport-limited vs. reaction-limited) is controlled by the parameter

$$G = \frac{2k\langle h_0 \rangle}{DSh} = \frac{PeDa}{Sh}. \quad \ldots\ldots (17)$$

Another important parameter is the ratio of the total thickness of the carbonate lamina to the initial aperture of the fracture,

$$\Delta = \frac{\langle h_c^u + h_c^l \rangle}{\langle h_0 \rangle} = \frac{\langle h_{\max} - h_0 \rangle}{\langle h_0 \rangle}, \quad \ldots\ldots (18)$$

following the notation of **Fig. 3.** Finally, the fifth parameter is the acid-capacity number,

$$\gamma = \frac{c_{\text{in}}}{c_{\text{sol}}}, \quad \ldots\ldots (19)$$

which gives the volume of solid dissolved by a unit volume of reactant. In Eq. 19, c_{in} is the initial concentration of the injected acid. In our case, $\gamma \approx 0.03$, taking $c_{\text{in}} = 0.83$ mol/cm^3, which corresponds to a 3% solution of hydrochloric acid (HCl).

As shown in Szymczak and Ladd (2012), whenever $\gamma \ll 1$, the time derivatives in Eqs. 2 and 3 can be dropped. Physically, this corresponds to an observation that c and $\mathbf{v}$ relax to their stationary values over a much faster time scale than that of a geometry change caused by the dissolution.

The final form of the equations for the fracture dissolution is then given by

$$\mathbf{q}(x,y,t) = -\frac{h^3(x,y,t)}{12\mu} \nabla p(x,y,t), \quad \nabla \cdot \mathbf{q}(x,y,t) = 0 \quad \ldots\ldots (20)$$

$$\mathbf{q} \cdot \nabla c - \nabla \cdot (hD \nabla c) = 2k_{\text{eff}} c \theta(h_{\max} - h), \quad \ldots\ldots (21)$$

$$c_{\mathrm{sol}}\frac{\partial h(x,y,t)}{\partial t} = 2k_{\mathrm{eff}}c\theta(h_{\max} - h). \quad (22)$$

Eqs. 20, 21, and 22 are solved using the finite-difference *porous* package, developed by Upadhyay and Ladd in Upadhyay et al. (2015), which uses finite-difference methods with a parallel multigrid linear solver *Hypre* (Falgout and Yang 2002).

(a) (b)

Fig. 3—Schematic of a fracture: (a) side view and (b) top view.

We use a regular grid of points in two dimensions with the lattice constant (pixel size) δl. In principle, the pixel size should be significantly smaller than the lateral offset, δx_l, used during the fracture synthesis. This is because the mismatch between the fracture surfaces over the length scales $l \leq \delta x_l$ is largely responsible for the overall roughness of the fracture. Failure to include these length scales results in unrealistically smooth fractures. However, choosing too small a value of δl will preclude us from simulating field-scale fractures because of computational limitations. To get around this difficulty, we first generate the fracture, surface $S_l(x,y)$ on a large grid, 65,536×65,536 pixels with pixel size $\delta l = \frac{1}{16}\delta x_l$. Next, we coarse grain this grid, by taking every 16th point in each direction, $S_l(16i\delta l, 16j\delta l)$, with $i, j \in (1, 4096)$. Finally, we modify the resulting aperture field by randomly adding or subtracting the standard deviation of the 16×16 array of S_l values of the finer grid centered around the respective points of the coarser grid. This procedure gives the roughness of the coarse aperture field within 10 to 20% of the roughness of the respective fine field.

As a result, we obtain the aperture field on a 4,096×4,096 grid with a pixel size of $\delta x = 0.1$ mm. This gives the linear size of fracture of approximately 40 cm (i.e., in the range of the distance between the individual fractures in the Pomeranian shales), as reported above.

The relative roughness of the initial aperture field of the fracture is defined as

$$\sigma = \frac{\sqrt{\langle h_0^2 \rangle - \langle h_0 \rangle^2}}{\langle h_0 \rangle}. \quad (23)$$

For the fracture geometry generated as described above (spectral synthesis with $H = 0.3$, mapping a fine grid on a coarse one, lateral shift by 0.1 mm followed by a vertical shift to obtain 20% contact area), the relative roughness has been measured to be $\sigma = 0.56$.

In most of the paper, we concentrate on the dissolution by HCl, with $k = 0.2$ cm/s (at 0.5 M) and the diffusion constant $D = 4.5 \times 10^{-5}$ cm^2/s (Fredd and Fogler 1998a; Economides and Nolte 2000). For such a high reaction rate, the parameter $G = 2kh/DSh \approx 10$; thus, the reaction is transport-limited, and $k_{\mathrm{eff}} = \dfrac{DSh}{2h}$ in Eqs. 21 and 22. Later, we will also consider dissolution in the presence of calcium chelating agents—in these cases, the dissolution rate is lower, and for a general expression for k_{eff}, Eq. 11 should be used.

The above-described numerical model of the acidization process is rather simple and neglects a number of potentially important factors. As far as the surface chemical kinetics is concerned, we have assumed a one-component, linear reaction, (Eq. 6) with a pH-independent reaction rate, which is an approximation of the real kinetics of a more complex process, which should hold at a relatively low pH (Plummer et al. 1978). Note that in the case of HCl, potential nonlinearities in the surface kinetics will not affect the overall dissolution dynamics because, as remarked above, the reaction is then transport-limited and controlled by diffusion only.

Moreover, we have neglected the presence of other components of the acidizing fluids, such as surface-active agents, iron-control agents, clay stabilizers, or emulsion breakers. Nevertheless, analogous one-component models have been used previously to describe wormhole formation in matrix acidizing (Hoefner and Fogler 1988; Fredd and Fogler 1998a; Golfier et al. 2002; Panga et al. 2005; Kalia and Balakotaiah 2007; Cohen et al. 2008; Maheshwari et al. 2013; Maheshwari and Balakotaiah 2013), and turned out to be rather successful in predicting both the quantitative and qualitative characteristics of the emerging dissolution pattern. In particular, they were shown to predict correctly the optimal acid injection rate that leads to the breakthrough at minimal expense of reactant.

Results

Characteristic Dissolution Time. An important time scale characterizing our system is the time it takes for the carbonate lamina to be completely dissolved at the upstream part of the fracture, which we will denote as τ_d. For the HCl, by integrating Eq. 22 with $k_{\mathrm{eff}} = \dfrac{DSh}{2h}$, one obtains

$$\tau_d = \frac{c_{\mathrm{sol}}}{2DShc_{\mathrm{in}}}\left(h_{\max}^2 - h_0^2\right) = \frac{h_{\max}^2 - h_0^2}{2DSh\gamma}. \quad (24)$$

The values of τ_d depend strongly on the total amount of calcite to dissolve, and vary from seconds for very thin carbonate lamina (of the order of 0.01 mm), to minutes for $h_c \approx 0.1$ mm, which is a characteristic value for the Pomeranian shales, and up to hours for thick layers (of the order of a millimeter).

1D Profiles for a Smooth Fracture: Stationary Solutions. Let us now consider the dissolution of a single fracture, assuming that all the physical fields are dependent only on a single spatial variable, x-distance from the inlet along the flow direction. The geometry of the system is then described by its 1D aperture profile, $h(x, t)$. For the moment, we assume that initially the fracture was smooth, $h(x, y, t = 0) \equiv h_0$, and that the carbonate lamina has a uniform thickness [i.e., $h_{\max}(x,y) = \text{constant}$]. In such a case, after the initial transient, we expect a uniform front to develop, propagating with velocity U, which can be determined by a mass balance of the reactant

$$U = \frac{\gamma q_0}{(h_{\max} - h_0)}. \quad \ldots\ldots (25)$$

On the basis of Eq. 25, a characteristic time for the front propagation can be defined as the time it takes for the front to move over the distance h_0; i.e.,

$$\tau_f = \frac{h_0}{U} = \frac{h_0(h_{\max} - h_0)}{\gamma q_0}. \quad \ldots\ldots (26)$$

To find the aperture and concentration profiles in the fracture after a long time ($t \gg \tau_d$), we transform the system of coordinates to the frame moving with the front, $x' = x - Ut$, with an origin at the front position (i.e., at the rightmost point where $h = h_{\max}$). The stationary concentration and aperture profiles are then the solutions of

$$q_0 \frac{\mathrm{d}c}{\mathrm{d}x'} = -\frac{DSh}{h} c \quad \ldots\ldots (27)$$

$$-U c_{\mathrm{sol}} \frac{\mathrm{d}h}{\mathrm{d}x'} = \frac{DSh}{h} c, \quad \ldots\ldots (28)$$

where again a transport-limited kinetics corresponding to HCl has been assumed. An immediate conclusion from Eqs. 27 and 28 is that the aperture and concentration are proportional to each other:

$$\hat{h}(x') \equiv \frac{h(x') - h_0}{h_{\max} - h_0} = \frac{c(x')}{c_{\mathrm{in}}}. \quad \ldots\ldots (29)$$

Putting this back into Eq. 27 and solving for $h(x)$ leads to

$$\frac{h(x)}{h_0} = 1 + W\left(\Delta e^{\Delta - \frac{Sh}{Pe}\frac{x'}{h_0}}\right), \quad \ldots\ldots (30)$$

where W is the Lambert W-function (Veberič 2012). **Fig. 4** presents the resulting 1D aperture profiles for several different Δ values. There are two things to be noted here. First, for small Δ, the rescaled profiles $\frac{h - h_0}{h_{\max} - h_0}$ converge to the Δ-independent asymptote,

$$\frac{h - h_0}{h_{\max} - h_0} = e^{-\frac{Sh}{Pe}\frac{x'}{h_0}}, \quad \ldots\ldots (31)$$

which can be obtained from Eq. 30 using the small-z asymptotics of the Lambert function, $W(z) \approx z$. On the other hand, for large Δ, the profiles become linear,

$$\frac{h - h_0}{h_{\max} - h_0} = 1 - \frac{Sh}{Pe}\frac{x'}{h_0}, \quad \ldots\ldots (32)$$

where the large-z asymptotics of the Lambert function, $W(z) \approx \log z - \log\log z$, has been used. The dependence of the profiles on the Péclet number comes down to a simple rescaling of the x-coordinate.

The aim of acidization of the cemented fractures is to expose a maximum area of shale at a minimum expenditure of acid. Thus, the aperture profiles should be kept as steep as possible; otherwise, the reactant will be wasted on the creation of long tails (see the case of $\Delta = 30$ in Fig. 4). This suggests that the Péclet number should not be excessive, as otherwise, the dissolution, although far-reaching, will be relatively shallow, and the matrix will not be exposed.

2D Effects: Unstable Growth and Wormhole Formation. The concentration and aperture profiles obtained in the preceding subsection are derived under the assumption that all the relevant quantities depend only on a single spatial variable: the distance from the inlet. The underlying picture is then that of an initially smooth fracture that opens uniformly along its width. However, the dissolution process is known to be unstable, because of the positive feedback between the flow, reactant transport, and geometry evolution: A relatively small change in fracture aperture caused by the dissolution may result in a variation of permeability, focusing the flow and leading to further changes in erosion. As a result, small inhomogeneities in the initial aperture field tend to grow and get transformed into highly permeable, finger-like flow channels called wormholes. The fact that the wormholes can form in the dissolution of porous media has been known in the petroleum industry for a long time (Rowan 1959), but the theoretical description of the reactive-infiltration instability was developed only in the 1980s (Chadam et al. 1986; Ortoleva et al. 1987; Hinch and Bhatt 1990). These papers have focused exclusively on a dissolving porous media; however, the fractures are also known to dissolve nonuniformly, with wormhole formation, as shown numerically by Rajaram and coworkers (Hanna and Rajaram 1998; Cheung and Rajaram 2002) and experimentally by Detwiler et al. (2003). The corresponding theory for the reactive-infiltration instability in fractures has been developed subsequently (Szymczak and Ladd 2012) and verified experimentally by Osselin et al. (2016). Importantly, it has been shown that the dissolution in the fracture

can be unstable both in the case of unlimited aperture growth and in the case where the aperture of the fracture cannot grow indefinitely (Szymczak and Ladd 2013). The former case corresponds to the dissolution of a narrow fracture in a large block of completely soluble material (e.g., limestone rock), a classical problem in the studies of cave and karst formation. The latter problem is that of a fracture in a thin layer of cement in otherwise insoluble rock (i.e., the case of direct relevance here).

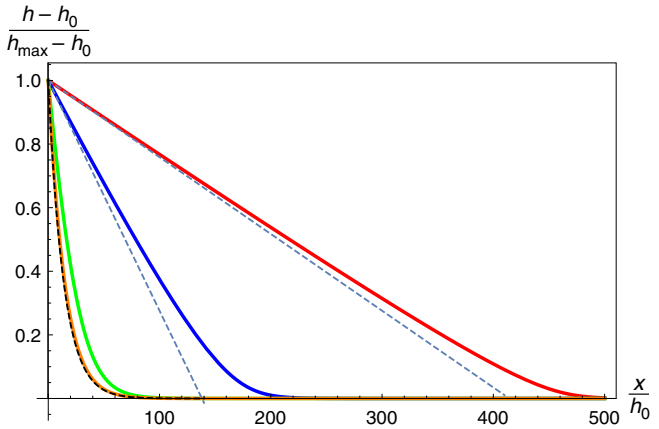

Fig. 4—Profiles of the rescaled aperture, $\langle \hat{h} \rangle$ for *Pe* = 100 and different lamina thicknesses: $\Delta = 0.1$ (orange), $\Delta = 1$ (green), $\Delta = 10$ (blue), and $\Delta = 30$ (red). The large-Δ asymptotics, as given by Eq. 32, is marked by gray dashed lines, whereas the small-Δ asymptotics, given by Eq. 31, is marked by a black dashed line.

Even though it was shown theoretically that the dissolution in laminated fractures is unstable, the corresponding wormhole-formation process has not been studied. The only exception is the paper by Budek et al. (2017), which, however, focused on highly idealized, smooth fracture geometries with the aim of understanding the dynamics of interactions between the dissolution fingers. Here, instead, we focus on realistic, self-affine, rough geometries of reactivated fractures in shales, generated from the power spectra (Eq. 1). In such cases, the dissolution patterns will be controlled both by the distinctive features of the initial aperture distribution and by the instability mechanism. The wormhole patterns arising in such a case are illustrated in **Fig. 5.** As the figure shows, the patterns depend strongly on the lamina thickness. For small Δ, the wormholes are diffuse, and they merge easily with each other, forming a wavy, yet relatively uniform, reaction front. Then, as Δ is increased, the ratio between finger width and the distance between the fingers decreases, which results in better-defined fingers, deeply etched in the carbonate cement. Finally, at $\Delta \geq 10$, the fingers are thin and highly branched, which gives the pattern a fractal character. Another phenomenon, well-visible at large Δ, is a strong competition between the fingers, with the longer ones screening the shorter ones off and intercepting their flow. The fingers repel in this regime and never touch. Contrastingly, at intermediate Δ, the interaction between the fingers is more complex—the fingers of similar length repel, but at the same time, shorter fingers get attracted to the base of the longer ones, which produces characteristic looped structures with islands of undissolved lamina surrounded by the dissolved regions. The attraction between the fingers can be understood based on the analysis of the pressure field around them (Szymczak and Ladd 2006; Budek et al. 2017). The pressure gradient in the longer finger is steeper than in the shorter one because the flow rate is higher in the longer finger. As a result, there is a pressure difference between the tip of the shorter finger and the body of the longer one, with the flow directed toward the longer finger. Such a flow pattern is a characteristic feature of fingered growth systems, observed experimentally both in fracture dissolution and in viscous fingering patterns (Detwiler et al. 2003; Budek et al. 2015). This effect increases in magnitude with the difference in length between the interacting fingers; this is why it is usually most pronounced in the later stages of the dissolution (see **Fig. 6**), where the contrasts in length between the fingers become appreciable.

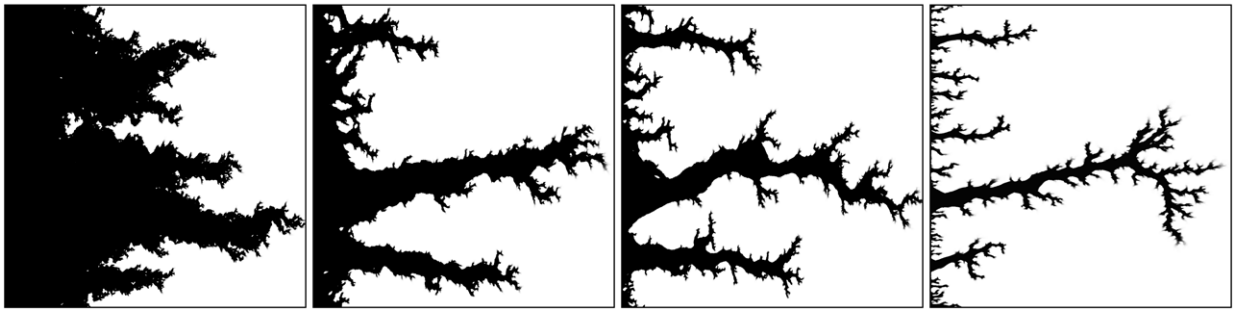

Fig. 5—HCl dissolution patterns in the laminated fractures at *Pe* = 100 for different lamina thicknesses: $\Delta = 0.33$, $\Delta = 1.5$, $\Delta = 3$, and $\Delta = 15$ (from left to right). The dissolved region is marked in black. The patterns are recorded at the breakthrough time, when the longest channel reaches the end of the system.

Another marked difference between the patterns at different Δ values is the appearance of the completely dissolved area behind the front for small Δ (black region in Fig. 5). The extent of this region gets progressively smaller with an increase of Δ, and it vanishes completely in the hierarchical growth regime for $\Delta > 10$.

On a more quantitative level, we can characterize these patterns by two parameters. The first, $s(\Delta)$, is defined as a fraction of the fully dissolved area in the system at breakthrough (i.e., at the moment when the longest finger reaches the outlet). By analogy with

fluid/fluid displacement theory, we can call it "sweep efficiency." The second quantity, $b(\Delta)$, is given by the fraction of the undissolved ("bypassed") area (in practice, we count as such the area in which the aperture has grown by less than 0.05 h_c). **Fig. 7** shows the dependence of these parameters on the lamina thickness. Note that $s+b<1$ because neither of these measures accounts for partially dissolved regions. As already mentioned, the acidization of cemented shale fractures serves two purposes: We strive to uncover as large an area of the shale matrix as possible, at the same time trying to keep some of the carbonate lamina intact to support the fracture against the load. The former task is equivalent to maximizing *s,* whereas the latter task requires maximizing *b*. As shown in Fig. 7, the two goals cannot be achieved simultaneously. Small lamina thicknesses will result in uniform dissolution that will fail to prevent the closure of the fracture under the overburden, whereas very large thicknesses hinder the uncovering of the shale matrix.

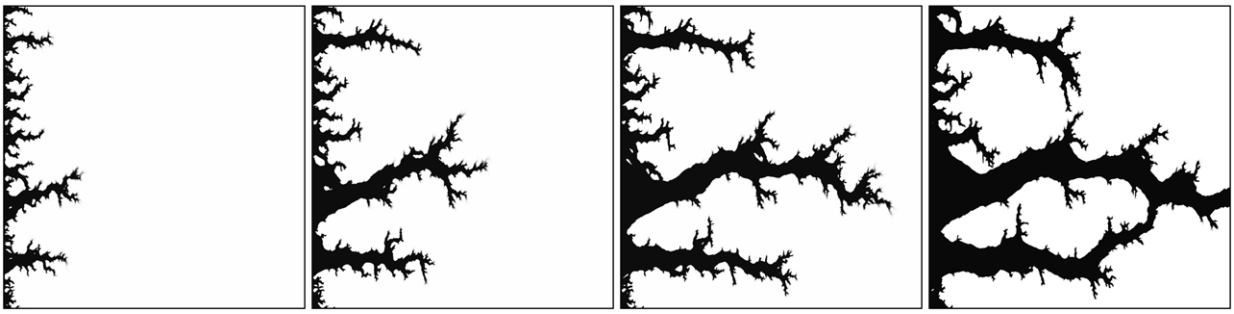

Fig. 6—HCl dissolution patterns in the laminated fractures for Δ = 3 at four different moments of time.

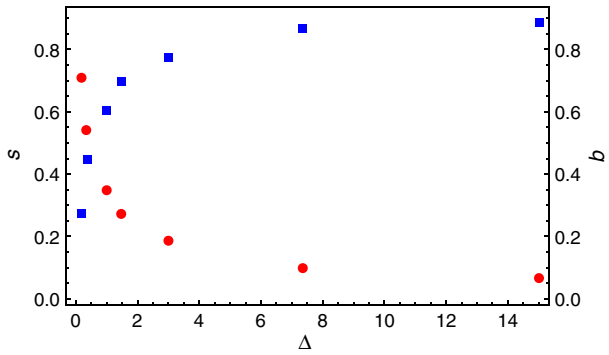

Fig. 7—The sweep efficiency (*s*, red circles) and the bypassed fraction (*b*, blue squares) as a function of the relative lamina thickness, Δ.

All the patterns in Figs. 5 and 6 have been obtained with the same random aperture field, just shifted to achieve different Δ values. The rationale behind such an approach was to focus on the effects of the lamina thickness on the dissolution patterns. However, for a given Δ, the wormhole pattern would still depend on a realization of a random field that describes the initial aperture, as illustrated in **Fig. 8** for $\Delta=3$. As observed, even though wormholes appear in different places, the statistical features of the pattern remain the same. The features in question include the thickness of the main wormhole, the length ratio of the longest wormhole to the second-longest, or the sweep efficiency (the latter differs by a few percent only—it is equal to 0.194 for the pattern in the left panel of Fig. 8, and 0.201 for the pattern in the right panel).

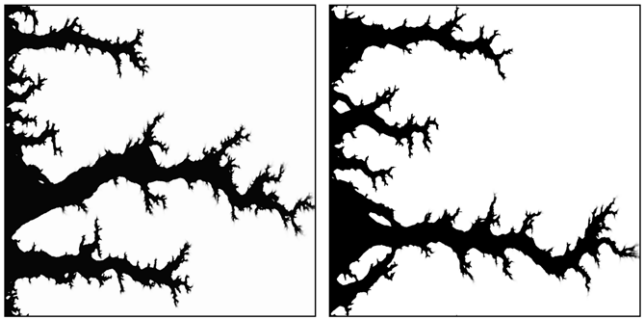

Fig. 8—The dissolution patterns for Δ = 3 for two different realizations of the final random aperture field.

The Influence of the Reaction Rate on the Dissolution Patterns: Weaker Acids and Chelating Agents

Thus far, we have focused on HCl, which is one of the most popular acidizing fluids. However, weaker acids and chelating agents also have been shown to be effective stimulation fluids. For example, 0.5-M acetic acid has the surface reaction rate of $k=5\times10^{-3}$ cm/s and the diffusion constant $D=1.1\times10^{-5}$ cm^2/s (Fredd and Fogler 1998a), which gives $G\approx1$, indicating a mixed regime with both

reaction and transport controlling to the dissolution process. Some of the calcium chelating agents dissolve limestone even more slowly [e.g., 0.25-M cyclohexanediaminetetraacetic acid (CDTA) with $k = 2.3\times10^{-4}$ cm/s and $D = 4.5\times10^{-6}$ cm^2/s, corresponding to $G \approx 0.1$ or 0.25-M diethylenetriaminepentaacetic acid (DTPA) with $k = 4.8\times10^{-5}$ cm/s and $D = 4\times10^{-6}$ cm^2/s (Fredd and Fogler 1998a), which gives $G \approx 0.03$. While simulating acidization in these cases, a more general expression (Eq. 11) for the effective dissolution rate should be used in place of Eq. 13 The resulting patterns would then depend on G, as illustrated in **Fig. 9.** The form of this dependence is far from trivial. As observed, when the transport parameter G is decreased to approximately 0.1, the competition between the wormholes is becoming weaker, and the number of longer wormholes increases. However, another trend is also present and becoming increasingly evident—as G decreases, the wormholes become straighter. This is because a lower reaction rate allows the reactant to survive longer, and thus explore more flow paths in the vicinity of the main flow channel. The reactive flow with such properties becomes more efficient in getting around the local asperities. This effect of a decreased tortuosity is the strongest in the main channel, where flow is highest. As a result, this channel is now even more effective in focusing the flow, and it kills off the competing channels more easily, as observed for $G = 0.01$ and $G = 0.001$. At the same time, the main channel becomes more diffuse for the same reason. Finally, at $G = 0.001$, the reaction rate becomes so low that the reactant penetration length is now comparable with the dimensions of the system and the dissolution pattern becomes uniform. Interestingly, because of the interplay of the two opposing trends (weaker competition between the channels due to the more uniform dissolution at smaller G and faster growth of the main channel due to its decreased tortuosity), the sweep efficiency of the patterns shown in Fig. 9 is almost constant in the range $\infty > G > 5\times10^{-3}$ with the value $s = 0.23 \pm 0.4$. Only after G decreases below 5×10^{-3} does the sweep efficiency begin to rise to reach $s = 0.54$ at $G = 0.001$ (the rightmost panel of Fig. 9). The practical conclusion to be drawn from this data is that the shale fractures also can be acidized by weaker acids with a similar range of sweep efficiencies expected.

Fig. 9—The dissolution patterns in laminated fractures for $\Delta = 3$ at different values of the transport parameter G (Eq. 17). From left to right: $G = \infty$, $G = 1$, $G = 0.1$, $G = 0.01$, and $G = 0.001$.

Again, a number of simplifying assumptions have been made here, most notably that the calcite dissolution by weaker acids and chelating agents can be described by first-order reaction. This is an effective model, approximating an overall effect of a large number of elementary reactions; thus, the reaction rate k will, in general, depend on the pH. As argued by Fredd and Fogler (1998a), such a model should be applicable for the dissolution induced by acetic acid (Fredd and Fogler 1998b). The same authors also have argued that a linear kinetic law can be used to describe the action of chelating agents if the relatively slight influence of product adsorption and site blocking is assumed negligible. It needs to be mentioned, however, that the applicability of these models has been subsequently questioned (Buijse et al. 2004; Alkhaldi et al. 2010), and a more complex kinetic model proposed. Moreover, in the present study, we have neglected the influence of the product transport on the overall dissolution rate, taking into account only the reactant transport. Although, in the case of HCl and chelating agents, the product transport can be neglected (Fredd and Fogler 1998a); for organic acids, it can play a more substantial role (Fredd and Fogler 1998b). Clearly, further study is needed regarding the influence of these factors on the dissolution patterns.

Discussion

The main result of the numerical simulations reported here is that the dissolution of carbonate lamina in shale fractures is expected to proceed in a highly nonuniform manner as a result of the reactive-infiltration instability. This instability stems from a positive-feedback loop between flow, transport, and erosion rate: a small perturbation to the dissolution front results in a locally increased flow rate, which, in turn, leads to increased dissolution, amplifying the perturbation.

Two features of the reactive-infiltration instability are relevant to the present discussion. The first is the fact that the positive-feedback loop between the flow and dissolution produces patterns across all the spatial scales: from the changes in the microstructure of the rock matrix and preferential opening of macropores [as observed in shales by Wu and Sharma (2015) and Grieser et al. (2007)], emergence of core-scale structures such as nonuniform etching of the fracture walls (Ruffet et al. 1998), or the formation of wormhole-like dissolution channels on the fracture surfaces (Dong et al. 1999; Detwiler et al. 2003; Szymczak and Ladd 2009) up to the macroscopic forms such as caves or solution pipes in the karst landscape (Ginés et al. 2009).

The second observation is that, although local inhomogeneities in the initial aperture will trigger the development of the localized flow paths and speed up the appearance of instability, the statistical properties of the emerging patterns on the large scale are largely insensitive to the initial geometry of the fracture (Upadhyay et al. 2015).

Most of the experimental studies of wormhole formation in fractures have dealt with limestone rocks (Durham et al. 2001; Ellis et al. 2011; Deng et al. 2013; Noiriel et al. 2013; Ishibashi et al. 2013; Smith et al. 2013; Elkhoury et al. 2013), which is fundamentally different from the present case, because the growth of the aperture in these systems is potentially unlimited. One exception is the work of Osselin et al. (2016), who studied the dissolution of a synthetic fracture created in a microfluidic cell, with a gypsum block inserted in between two polycarbonate plates (**Figs. 10a and 10b).** The geometry is thus analogous to that in Fig. 3, with the only difference being that the soluble material is present at one of the surfaces only. Osselin et al. (2016) demonstrate that even if initial aperture is almost ideally smooth (with the relative roughness of the order of 10^{-3}), the dissolution still proceeds in a nonuniform manner with the appearance of a well-defined instability wavelength. To mimic a much rougher appearance of the shale fractures, we have repeated this experiment by directly placing the upper polycarbonate plate on a gypsum block, instead of using a 70-μm spacer, as is the case in Osselin et al. (2016). Profilometry measurements (using Bruker contour GT-K0 profilometer with 5X objective) have allowed us to

estimate the aperture in this case to be $h_0 = 20$ μm while $\sigma \approx 0.5$. The thickness of the gypsum chip used in the experiment is 500 μm, thus $\Delta \approx 25 \gg 1$. For such Δ, the simulations predict a fractal-dissolution pattern with a strong differentiation between the fingers caused by screening, and it is indeed observed in the experiment (Fig. 10c). Although the qualitative resemblance of these patterns to their counterparts in Fig. 4 is rather striking, a note of caution is needed because this is a model system (gypsum on polycarbonate + water) and not the real one (calcite on shale + HCl). However, the dissolution kinetics of gypsum in water is linear (Colombani 2008), analogously to the calcite dissolution kinetics at low pH. Still, gypsum under these conditions dissolves under mixed rather than transport-limited kinetics, with the transport parameter $G = 0.05$. On the other hand, the data in Fig. 9 suggest that the differences between the dissolution patterns at different G are rather small.

At this point, it is worth discussing an important paper (Tripathi and Pournik 2014) that reports that the conductivity of acidized shale fractures actually decreases after the acidization. This has been attributed to the significant weakening of the shale matrix resulting from acidization and subsequent closure of the fracture under loading.

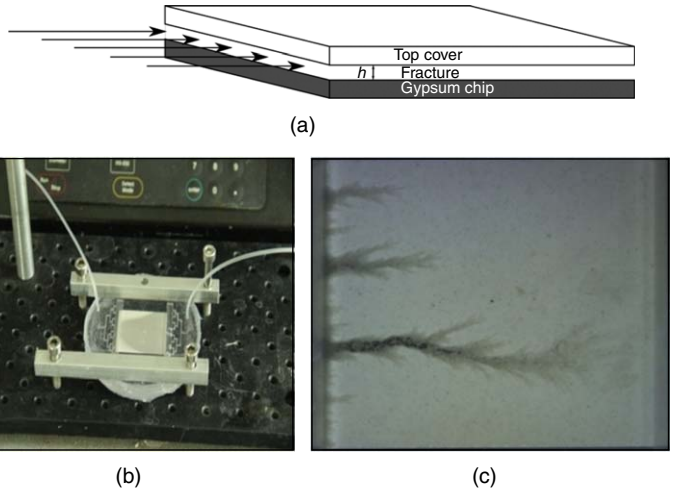

Fig. 10—The microfluidic experiment on the dissolution of synthetic gypsum fracture obtained by matching a soluble gypsum plate with a polycarbonate plate—a schematic view (a), a photograph of the system (b), and the dissolution patterns for $\Delta = 25$ (c). Dark regions in the figure correspond to the dissolved areas of the gypsum block.

In fact, there are a number of important differences between the present case and that considered by Tripathi and Pournik (2014). First, we consider natural fractures with the carbonate mineralization related to the paleofluid circulation, whereas the fractures in experiments of Tripathi and Pournik (2014) have been newly created by cutting the cores. Accordingly, they were devoid of any carbonate precipitate, except for the calcite naturally occurring as a part of the shale matrix. Second, the mineralogical composition of shale matrix in Tripathi and Pournik (2014) revealed a very high (almost 60%) carbonate content, which means that HCl dissolution will dramatically change its porosity and compressive strength. Conversely, the carbonate content in the matrix of the Pomeranian shales under study is only 3 to 5%; thus, dissolution should not change their elastic properties in any appreciable manner. Third, Tripathi and Pournik (2014) have analyzed relatively short samples ($L \approx$ 5-cm length), whereas the acid injection rates were very high (30 mL/min), which, for a fracture width of 3.8 cm, gives $q_0 \approx 0.15$ cm^2/s or $Pe = 3 \times 10^3$. As shown in the analysis of 1D profiles (Eq. 30), the acid penetration length characterizing the dissolution patterns in this system is given by $l_p = \langle h_0 \rangle Pe/Sh$. For $\langle h_0 \rangle = 0.127$ cm, as reported in Tripathi and Pournik (2014), this leads to the penetration length of approximately $l_p = 50$ cm, an order of magnitude longer than the fracture length. As is known, for $L/l_p \gg 1$, the dissolution is expected to be uniform (Starchenko et al. 2016), and no large-scale inhomogeneities form. However, the fractures considered in the present work are characterized by much smaller apertures, and thus we expect to be in the regime $L \gg l_p$, which invariably involves wormhole formation.

As already mentioned, the acidization of cemented fractures serves two main purposes. First, it uncovers the shale matrix, thus providing a pathway for the methane transport from the formation toward the wellbore. Second, nonuniform dissolution results in an appearance of the areas of intact mineralization, which act as support points to keep more-dissolved regions open. The latter goal is arguably more important than the former, because it guarantees that the fracture remains a conductive part of the network, even if it does not take part in the production itself. Even a relatively small number of carbonate islands are able to keep the fracture open, as evidenced by the presence of mineral bridges supporting open shale fractures, even at a 3-km depth (see **Fig. 11**).

The extent to which these two goals can be achieved depends primarily on the thickness of the carbonate lamina relative to the initial aperture of the fracture, Δ. The estimation of this parameter for the Pomeranian shales is difficult, because it would, in principle, require an experiment on the recracking of the cemented fractures under reservoir conditions. Some clues, however, might be derived from the analysis of the mineralized fractures from the core, which have reopened during the core excavation. White-light interferometry scans of these samples reported in Pluymakers et al. (2017) reveal that the out-of-plane fluctuations of the calcite-covered fracture surfaces are of the order of 0.01 to 0.03 mm. However, the lamina thicknesses in the fractures fall in the range of 0.05 to 0.5 mm, with most of the values dispersed around 0.1 mm. This yields values of Δ in the range 1.5 to 50, with a typical value around 4. We can thus expect sweep efficiencies in the range 0.3 to 0.05, typically around 0.2. The bypassed fraction is in the range 0.7 to 1, which guarantees that the fracture will remain open.

Importantly, after the main channel breaks through, the total consumption of the reactant in the fracture dramatically decreases, as most of the acid is now transported directly to the outlet without reacting. Thus, the carbonate bridges formed during the initial stages of the dissolution will most likely be preserved in the later stages after the breakthrough.

The amount of acid needed for an effective stimulation of shale formations does not need to be excessive. In a proposal for the acidization treatment of Woodford shale, Grieser et al. (2007) suggest using six injections of 27 m^3 of 3% HCl. Such a volume is sufficient

for the dissolution of 5 m^3 of carbonate cement, which corresponds to approximately 1×10^5 m^3 of the shale volume, assuming a sweep efficiency of 0.2. This is comparable with the estimates of the stimulated reservoir volume for the Pomeranian shales, which is predicted to be of the order of $50\times50\times200$ m (i.e., 5×10^5 m^3), which implies that approximately 20% of veins would be treated. If needed, a larger volume of acidic fluid can be injected, which still is expected to be economically feasible in view of the anticipated increase of shale-gas production. A more concentrated HCl also can be used, in accordance with the acidization practice, where the acid concentrations are usually between 8 and 15%. The main effect of the increase of HCl concentration is the increase of the acid-capacity number (Eq. 19) and the associated decrease of characteristic dissolution times (Eqs. 24 and 26). Another effect of the more concentrated acid would be the increase of the reaction rate constant, k, which is pH-dependent (Pokrovsky et al. 2009). This effect will, however, not have any bearing on the dissolution patterns, because HCl dissolution is mass-transfer-limited and, thus, independent of the exact value of the reaction rate (see Eq. 13).

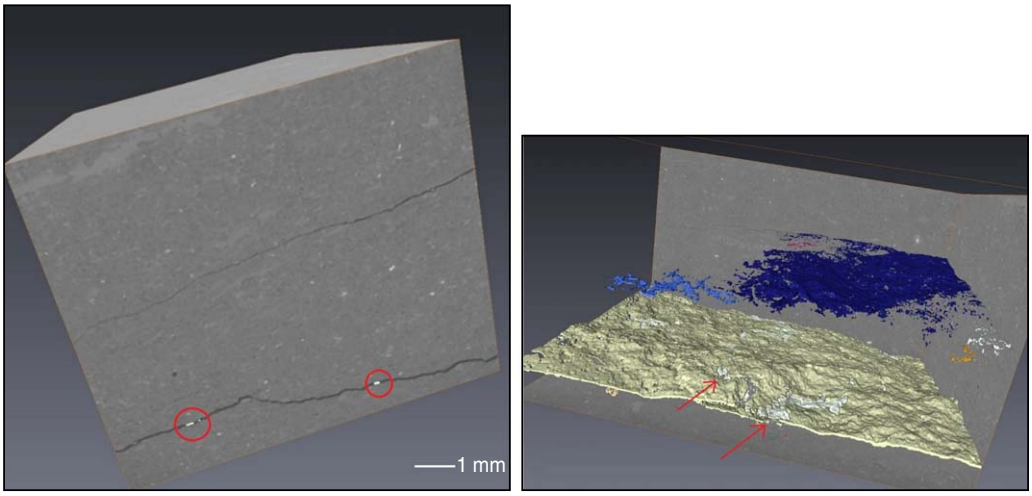

Fig. 11—Carbonate bridges supporting the open cracks in Vaca Muerta shale samples (Argentina) collected from a borehole at a 3-km depth (Ougier-Simonin et al. 2016). The samples were scanned in three-dimensions using X-ray microtomography at the European Synchrotron Radiation Facility, beamline ID19 and BM05, voxel size 0.62 μm. The photos are courtesy of Francois Renard, University of Grenoble Alpes.

Another possibility is to use a weaker acid or chelating agents for acidization instead of HCl. As shown above, the dissolution patterns in laminated fractures are only weakly dependent on the reaction rate in a rather wide range of rates. Only for reaction rates lower than $k=2\times10^{-5}$ cm/s do the dissolution patterns become significantly more diffuse, marking the transition to a uniform-dissolution regime (Hoefner and Fogler 1988; Golfier et al. 2002). A relatively weak dependence of the dissolution patterns on the reaction rate indicates a large degree of control of the patterns by the rough geometry of the initial, undissolved fracture, which largely determines the positions of growing wormholes.

Other media often used in acidization are diverting acids such as in-situ crosslinked acids or surfactant-based viscoelastic acids (MaGee et al. 1997; Gomaa et al. 2011; Ratnakar et al. 2013). Their viscosity increases with the pH; hence, their injection results in more uniform patterns. Initially, both the flow and dissolution focus in high-permeability regions. As a result, pH increases there, resulting in an increase of the viscosity of the fluid and the clogging of the wormholes. As a result, the aggressive fluid flows to less-permeable regions, and the dissolution patterns become more uniform. In the present case, however, this is not a desired outcome, because one strives to keep the patterns as ramified as possible, so that less-dissolved regions can act as supports to keep more-dissolved regions open. Hence, the use of diverting acids for the acidization of mineralized shale fractures is not recommended. Nevertheless, a certain degree of the mobility alteration might be unavoidable, because corrosion inhibitors or clay stabilizers that are usually contained in the treatment fluids can divert the acid to a certain extent.

Conclusions

The most important conclusion of the present study is that the dissolution of carbonate-cemented fractures by low-pH fluids proceeds in a highly inhomogeneous way, with the formation of highly localized flow paths. This has been confirmed both in the numerical simulations of acidization of laminated fractures and in the analog experiments with gypsum fractures.

Such an inhomogeneous dissolution turns out to be crucially important when acidizing carbonate-cemented fractures in shale formations. On the one hand, acidization will then help in getting rid of the carbonate lamina, which hinders the fracture/matrix transfer. On the other hand, heterogeneous dissolution patterns will help to sustain fluid flow, even when proppant is absent or crushed, preventing the resealing of the fracture as the fluid pressure is removed, because the less-dissolved regions will act as supports to keep the more-dissolved regions open. The formation of wormholes is beneficial in yet another way. Long and thin conduits can be used as bypasses between the wellbore and the hydraulically induced fractures, which are free of the lamina. Thus, even if the contribution of the natural fractures to the gas production is limited, they at least do not block the fluid pathway to the more productive parts of the formation.

Hence, acidization of the formation with a relatively large volume of HCl appears to be a necessity whenever the following three conditions are satisfied: (i) the density of the natural fractures in the formation is high, (ii) most of these fractures are cemented with a carbonate cement, and (iii) the stress conditions in the formation favor the opening of pre-existing fractures rather than the creation of new hydraulic-fracture pathways. These conditions are met in the case of the Pomeranian gas-bearing shale reservoir; thus, an extensive acidization of the reactivated fractures with HCl is essential for the effective production of shale gas from these formations. Favorably, mineralization volumes per unit volume of the rock are not excessive, which makes it possible to dissolve the carbonate cement in a

significant portion of stimulated reservoir volume with reasonable quantities of HCl. While we have focused on Pomeranian shales in this work, these conclusions should hold for other shale formations with mineralized fractures, provided that the fractures are numerous and the carbonate lamina is relatively thick compared with the aperture.

Nomenclature

b = bypassed area fraction
c = velocity-averaged concentration of H^+, mol/L^3
c_{in} = velocity-averaged concentration of H^+ at the inlet of the fracture, mol/L^3
c_{sol} = molar concentration of the solid phase, mol/L^3
D = diffusion coefficient, L^2/t
Da = Damköhler number
G = transport parameter
h = fracture aperture, L
h_0 = initial aperture of reactivated fracture, L
h_c = thickness of calcite lamina, L
H = the Hurst exponent
Pe = Péclet number
$\mathbf{q}$ = volume flux per unit length across the fracture, L^2/t
$\mathbf{s}$ = sweep efficiency
Sh = Sherwood number
U = dissolution front velocity, L/t
$\mathbf{v}$ = velocity field, L/t
γ = acid-capacity number
κ = wave number, 1/L
Δ = thickness of calcite lamina normalized by the initial aperture

Acknowledgments

Authors thank Kinga Bobek and Sylwester Salwa from the Polish Geological Institute for their help in preparation of figures. We benefited from discussions with Tony Ladd, Agnieszka Budek, and Paweł Kondratiuk; Virat Upadyhay and Tony Ladd are also acknowledged for their finite-difference code *porous,* which has been used in the simulations. We thank Polish Oil and Gas Company (PGNiG) for granting us access to the core and the data. This work was supported by the SHALESEQ project, funded by the Polish-Norwegian Research Programme operated by the National Centre for Research and Development under the Norwegian Financial Mechanism 2009–2014 (Contract No. POL-NOR/234198/100/2014).

References

Adler, P. M. and Thovert, J.-F. 2000. *Fractures and Fracture Networks*. Kluwer.

Alkhaldi, M. H., Nasr-El-Din, H. A., and Sarma, H. K. 2010. Kinetics of the Reaction of Citric Acid With Calcite. *SPE J.* **15** (3): 704–713. SPE-118724-PA. https://doi.org/10.2118/118724-PA.

Asef, M. and Farrokhrouz, M. 2013. *Shale Engineering: Mechanics and Mechanisms*. Taylor & Francis.

Bird, R. B., Stewart, W. E., and Lightfoot, E. N. 2001. *Transport Phenomena*. John Wiley & Sons.

Bons, P. D., Elburg, M. A., and Gomez-Rivas, E. 2012. A Review of the Formation of Tectonic Veins and Their Microstructures. *J. Struct. Geol.* **43:** 33–62. https://doi.org/10.1016/j.jsg.2012.07.005.

Brantley, S. L., Kubicki, J. D., and White, A. F. 2008. *Kinetics of Water-Rock Interaction*. Springer.

Brown, S. 1987. Fluid Flow Through Rock Joints: The Effect of Surface Roughness. *J. Geophys. Res.* **92** (B2): 1337–1347. https://doi.org/10.1029/JB092iB02p01337.

Budek, A., Garstecki, P., Samborski, A. et al. 2015. Thin-Finger Growth and Droplet Pinch-Off in Miscible and Immiscible Displacements in a Periodic Network of Microfluidic Channels. *Phys. Fluids* **27:** 112109. https://doi.org/10.1063/1.4935225.

Budek, A., Kwiatkowski, K., and Szymczak, P. 2017. Effect of Mobility Ratio on Interaction Between the Fingers in Unstable Growth Processes. *Phys. Rev. E* **96:** 042218. https://doi.org/10.1103/PhysRevE.96.042218.

Buijse, M., de Boer, P., Breukel, B. et al. 2004. Organic Acids in Carbonate Acidizing. *SPE Prod & Fac* **19** (3): 128–134. SPE-82211-PA. https://doi.org/10.2118/82211-PA.

Chadam, D., Hoff, D., Merino, E. et al. 1986. Reactive Infiltration Instabilities. *IMA J. Appl. Math.* **36:** 207–221.

Cheung, W. and Rajaram, H. 2002. Dissolution Finger Growth in Variable Aperture Fractures: Role of the Tip-Region Flow Field. *Geophys. Res. Lett.* **29:** 2075. https://doi.org/10.1029/2002GL015196.

Cohen, C., Ding, D., Quintard, M. et al. 2008. From Pore Scale to Wellbore Scale: Impact of Geometry on Wormhole Growth in Carbonate Acidization. *Chem. Eng. Sci.* **63:** 3088–3099. [Also in *Chem. Eng. Sci.* **64** (12) 3029–3030] https://doi.org/10.1016/j.ces.2009.02.048.

Colombani, J. 2008. Measurement of the Pure Dissolution Rate Constant of a Mineral in Water. *Geochim. Cosmochim. Acta* **72:** 5634–5640. https://doi.org/10.1016/j.gca.2008.09.007.

Curtis, J. B. 2002. Fractured Shale-Gas Systems. *AAPG Bull.* **11:** 1921–1938. https://doi.org/10.1306/61EEDDBE-173E-11D7-8645000102C1865D.

Daneshy, A. 2016. Mechanics of Natural Fracture Activation by Hydraulic Fracturing. *Hydraul. Fract. J.* **3:** 8–21.

Deng, H., Ellis, B. R., Peters, C. A. et al. 2013. Modifications of Carbonate Fracture Hydrodynamic Properties by Co_2-Acidified Brine Flow. *Energy & Fuels* **27** (8): 4221–4231. https://doi.org/10.1021/ef302041s.

Detwiler, R. L., Glass, R. J., and Bourcier, W. L. 2003. Experimental Observations of Fracture Dissolution: The Role of Péclet Number in Evolving Aperture Variability. *Geophys. Res. Lett.* **30:** 1648. https://doi.org/10.1029/2003GL017396.

Detwiler, R. 2010. Permeability Alteration Due to Mineral Dissolution in Partially Saturated Fractures. *J. Geophys. Res.* **115:** B09210. https://doi.org/10.1029/2009JB007206.

Dijk, P. and Berkowitz, B. 1998. Precipitation and Dissolution of Reactive Solutes in Fractures. *Water Resour. Res.* **34** (3): 457–470. https://doi.org/10.1029/97WR03238.

Dijk, P., Berkowitz, B., and Yechieli, Y. 2002. Measurement and Analysis of Dissolution Patterns in Rock Fractures. *Water Resour. Res.* **38:** 1013. https://doi.org/10.1029/2001WR000246.

Dong, C., Hill, A., Zhu, D. et al. 1999. Acid Etching Patterns in Naturally-Fractured Formations. Presented at the SPE Annual Technical Conference and Exhibition, Houston, 3–6 October. SPE-56531-MS. https://doi.org/10.2118/56531-MS.

Dreybrodt, W. 1990. The Role of Dissolution Kinetics in the Development of Karst Aquifers in Limestone: A Model Simulation of Karst Evolution. *J. Geol.* **98** (5): 639–655. https://doi.org/10.1086/629431.

Durham, W. B., Bourcier, W. L., and Burton, E. A. 2001. Direct Observation of Reactive Flow in a Single Fracture. *Water Resour. Res.* **37:** 1–12. https://doi.org/10.1029/2000WR900228.

Ebadian, M. A. and Dong, Z. F. 1998. Forced Convection, Internal Flow in Ducts. In *Handbook of Heat Transfer*, ed. W. M. Rohsenow, J. P. Hartnett, and Y. I. Cho. McGraw-Hill.

Economides, M. J. and Nolte, K. G. 2000. *Reservoir Stimulation*. John Wiley and Sons.

Elkhoury, J. E., Ameli, P., and Detwiler, R. L. 2013. Dissolution and Deformation in Fractured Carbonates Caused by Flow of CO_2-Rich Brine Under Reservoir Conditions. *Int. J. Greenh. Gas Con.* **16:** S203–S215. https://doi.org/10.1016/j.ijggc.2013.02.023.

Elkhoury, J., Detwiler, R., and Ameli, P. 2015. Can a Fractured Caprock Self-Heal? *Earth Planet. Sci. Lett.* **417:** 99–106. https://doi.org/10.1016/j.epsl.2015.02.010.

Ellis, B. R., Peters, C. A., Fitts, J. P. et al. 2011. Deterioration of a Fractured Carbonate Caprock Exposed to CO_2-Acidified Brine Flow. *Greenh. Gases* **1** (3): 248–260. https://doi.org/10.1002/ghg.25.

Falgout, R. D. and Yang, U. M. 2002. Hypre: A Library of High-Performance Preconditioners. In *International Conference on Computational Science*, pp. 632–641. Springer.

FracFocus 2017. Chemical Disclosure Registry, available at www.fracfocus.org.

Fredd, C. N. and Fogler, H. S. 1998a. Influence of Transport and Reaction on Wormhole Formation in Porous Media. *AIChE J.* **44** (9): 1933–1949. https://doi.org/10.1002/aic.690440902.

Fredd, C. N. and Fogler, H. S. 1998b. The Kinetics of Calcite Dissolution in Acetic Acid Solutions. *Chem. Eng. Sci.* **53** (22): 3863–3874. https://doi.org/10.1016/S0009-2509(98)00192-4.

Frenier, W. W. and Ziauddin, M. 2008. *Formation, Removal, and Inhibition of Inorganic Scale in the Oilfield Environment*. Richardson, Texas: Society of Petroleum Engineers.

Gale, J. F. W., Reed, R. M., and Holder, J. 2007. Natural Fractures in the Barnett Shale and Their Importance for Hydraulic Fracture Treatments. *AAPG Bull.* **91** (4): 603–622. https://doi.org/10.1306/11010606060.

Gale, J. F., Laubach, S. E., Olson, J. E. et al. 2014. Natural Fractures in Shale: A Review and New Observations. *AAPG Bull.* **98** (11): 2165–2216. https://doi.org/10.1306/08121413151.

Gandossi, L. 2013. An Overview of Hydraulic Fracturing and Other Formation Stimulation Technologies for Shale Gas Production. JRC Technical Report EUR 26347 EN, European Commission, Joint Research Centre, Institute for Energy and Transport.

Garcia-Rios, M., Luquot, L., Soler, J. M. et al. 2015. Influence of the Flow Rate on Dissolution and Precipitation Features During Percolation of CO_2-Rich Sulfate Solutions Through Fractured Limestone Samples. *Chem. Geol.* **414:** 95–108. https://doi.org/10.1016/j.chemgeo.2015.09.005.

Gasparrini, M., Sassi, W., and Gale, J. F. 2014. Natural Sealed Fractures in Mudrocks: A Case Study Tied to Burial History From the Barnett Shale, Fort Worth Basin, Texas. *March Petrol. Geol.* **55:** 122–141. https://doi.org/10.1016/j.marpetgeo.2013.12.006.

Ghommem, M., Zhao, W., Dyer, S. et al. 2015. Carbonate Acidizing: Modeling, Analysis, and Characterization of Wormhole Formation and Propagation. *J. Petrol. Sci. Eng.* **131:** 18–33. https://doi.org/10.1016/j.petrol.2015.04.021.

Ginés, A., Knez, M., Slabe, T. et al. 2009. *Karst Rock Features: Karren Sculpturing*. Zalozba ZRC.

Golfier, F., Zarcone, C., Bazin, B. et al. 2002. On the Ability of a Darcy-Scale Model To Capture Wormhole Formation During the Dissolution of a Porous Medium. *J. Fluid Mech.* **457:** 213–254. https://doi.org/10.1017.S0022112002007735.

Gomaa, A. M., Mahmoud, M. A., and Nasr-El-Din, H. A. 2011. Laboratory Study of Diversion Using Polymer-Based In-Situ-Gelled Acids. *SPE Prod & Oper* **26** (3): 278–290. SPE-132535-PA. https:/doi.org/10.2118/132535-PA.

Grieser, W. V., Wheaton, W. E., Magness, W. D. et al. 2007. Surface Reactive Fluid's Effect on Shale. Presented at the 2007 SPE Production and Operations Symposium, Oklahoma City, Oklahoma, 31 March–3 April. SPE-106815-MS. https://doi.org/10.2118/106815-MS.

Gupta, N. and Balakotaiah, V. 2001. Heat and Mass Transfer Coefficients in Catalytic Monoliths. *Chem. Eng. Sci.* **56** (16): 4771–4786. https://doi.org/10.1016/50009-2509(01)00134-8.

Hanna, R. B. and Rajaram, H. 1998. Influence of Aperture Variability on Dissolutional Growth of Fissures in Karst Formations. *Water Resour. Res.* **34:** 2843–2853. https://doi.org/10.1029/98WR01528.

Hao, Y., Smith, M., Sholokhova, Y. et al. 2013. CO_2-Induced Dissolution of Low-Permeability Carbonates. Part II: Numerical Modeling of Experiments. *Adv. Water Res.* **62:** 388–408. https://doi.org/10.1016/j.advwatres.2013.09.009.

Hinch, E. J. and Bhatt, B. S. 1990. Stability of an Acid Front Moving Through Porous Rock. *J. Fluid Mech.* **212:** 279–288. https://doi.org/10.1017/S0022112090001863.

Hoefner, M. L. and Fogler, H. S. 1988. Pore Evolution and Channel Formation During Flow and Reaction in Porous Media. *AIChE J.* **34:** 45–54.

Hung, K. M., Hill, A. D., and Spehrnoori, K. 1989. A Mechanistic Model of Wormhole Growth in Carbonate Acidizing and Acid Fracturing. *J Pet Technol* **41** (1): 59–66. SPE-16886-PA. https://doi.org/10.2118/16886-PA.

Imber, J., Armstrong, H., Clancy, S. et al. 2014. Natural Fractures in a United Kingdom Shale Reservoir Analog, Cleveland Basin, Northeast England. *AAPG Bull.* **98** (11): 2411–2437. https://doi.org/10.1306/0714113144.

Ishibashi, T., McGuire, T., Watanabe, N. et al. 2013. Permeability Evolution in Carbonate Fractures: Competing Roles of Confining Stress and Fluid pH. *Water Resour. Res.* **49** (5): 2828–2842. https://doi.org/10.1002/wrcr.20253.

Kalfayan, L. 2008. *Production Enhancement With Acid Stimulation*. Pennwell Books.

Kalia, N. and Balakotaiah, V. 2007. Modeling and Analysis of Wormhole Formation in Reactive Dissolution of Carbonate Rocks. *Chem. Eng. Sci.* **62:** 919–928. https://doi.org/10.10.1016/j.ces.2006.10.021.

Li, B. 2014. Natural Fractures in Unconventional Shale Reservoirs in US and Their Roles in Well Completion Design and Improving Hydraulic Fracturing Stimulation Efficiency and Production. Presented at the SPE Annual Technical Conference and Exhibition, Amsterdam, 27–29 October. SPE-170934-MS. https://doi.org/10.2118/170934-MS.

Liu, M., Zhang, S., and Mou, J. 2012. Fractal Nature of Acid-Etched Wormholes and the Influence of Acid Type on Wormholes. *Petrol. Explor. Devel.* **39** (5): 630–635. https://doi.org/10.1016/S1876-3804(12)60086-x.

Liu, M., Zhang, S., and Mou, J. 2013. Wormhole Propagation Behavior Under Reservoir Condition in Carbonate Acidizing. *Transp. Porous Med.* **96** (1): 203–220. https://doi.org/10.1007/s11242-012-0084-x.

MaGee, J., Buijse, M., Pongratz, R. et al. 1997. Method for Effective Fluid Diversion When Performing a Matrix Acid Stimulation in Carbonate Formations. Presented at the Middle East Oil Show, Bahrain, 15–18 March. SPE-37736-MS. https://doi.org/10.2118/37736-MS.

Maheshwari, P. and Balakotaiah, V. 2013. Comparison of Carbonate HCl Acidizing Experiments With 3D Simulations. Presented at the 2013 SPE Production and Operations Symposium, Oklahoma City, Oklahoma, 23–26 March. SPE-164517-MS. https://doi.org/10.2118/164517-MS. [Also, in *SPE Prod & Oper* **28:** (4): 402–413. SPE-164517-PA. https://doi.org/10.2118/164517-PA.]

Maheshwari, P., Ratnakar, R. R., Kalia, N. et al. 2013. 3D Simulation and Analysis of Reactive Dissolution and Wormhole Formation in Carbonate Rocks. *Chem. Eng. Sci.* **90:** 258–274. https://doi.org/10.1016/j.ces.2012.12.032.

Manchanda, R., Sharma, M. M., and Holzhauser, S. 2014. Time-Dependent Fracture-Interference Effects in Pad Wells. *SPE Prod & Oper* **29** (4): 274–287. SPE-164534-PA. https://doi.org/10.2118/164534-PA.

McDuff, D. R., Shuchart, C. E., Jackson, S. K. et al. 2010. Understanding Wormholes in Carbonates: Unprecedented Experimental Scale and 3D Visualization. *J Pet Technol* **62** (10): 78–81. SPE-129329-JPT. https://doi.org/10.2118/129329-JPT.

Menke, H. P., Bijeljic, B., Andrew, M. G. et al. 2015. Dynamic Three-Dimensional Pore-Scale Imaging of Reaction in a Carbonate at Reservoir Conditions. *Environ. Sci. Tech.* **49** (7): 4407–4414. https://doi.org/10.1021/es505789f.

Morsy, S., Sheng, J., Gomaa, A. M. et al. 2013a. Potential of Improved Waterflooding in Acid-Hydraulically-Fractured Shale Formations. Presented at the SPE Annual Technical Conference and Exhibition, New Orleans, 30 September 30–2 October. SPE-166403-MS. https://doi.org/10.2118/166403-MS.

Morsy, S. S., Sheng, J., and Soliman, M. 2013b. Improving Hydraulic Fracturing of Shale Formations by Acidizing. Presented at the SPE Eastern Regional Meeting, Pittsburgh, Pennsylvania, 20–22 August. SPE-165688-MS. https://doi.org/10.2118/165688-MS.

Morsy, S., Hetherington, C., and Sheng, J. 2015. Effect of Low-Concentration HCl on the Mineralogy, Physical, and Mechanical Properties, and Recovery Factors of Some Shales. *J. Unconv. Oil Gas Resour.* **9:** 94–102. https://doi.org/10.1016/j.juogr.2014.11.005.

Noiriel, C., Gouze, P., and Made, B. 2013. 3D Analysis of Geometry and Flow Changes in a Limestone Fracture During Dissolution. *J. Hydrol.* **486:** 211–223. https://doi.org/10.1016/j.jhydrol.2013.01.035.

Oron, A. P. and Berkowitz, B. 1998. Flow in Rock Fractures: The Local Cubic Law Assumption Reexamined. *Water Resour. Res* **34** (11): 2811–2825. https://doi.org/10.1029/98WR02285.

Ortoleva, P., Chadam, J., Merino, E. et al. 1987. Geochemical Self-Organization II: The Reactive-Infiltration Instability. *Am. J. Sc.* **287:** 1008–1040. https://doi.org/10.2475/ajs.287.10.1008.

Osselin, F., Budek, A., Cybulski, O. et al. 2016. Microfluidic Observation of the Onset of Infiltration Instability in an Analog Fracture. *Geophys. Res. Lett.* **43** (13): 6907–6915. https://doi.org/10.1002/2016GL069261.

Ott, H. and Oedai, S. 2015. Wormhole Formation and Compact Dissolution in Single- and Two-Phase CO_2-Brine Injections. *Geophys. Res. Lett.* **42** (7): 2270–2276. https://doi.org/10.1002/2015GL063582.

Ougier-Simonin, A., Renard, F., Boehm, C. et al. 2016. Microfracturing and Microporosity in Shales. *Earth-Sci. Rev.* **162:** 198–226. https://doi.org/10.1016/j.earscirev.2016.09.006.

Panga, M., Ziauddin, M., and Balakotaiah, V. 2005. Two-Scale Continuum Model for Simulation of Wormholes in Carbonate Acidization. *AIChE J.* **51** (12): 3231–3248. https://doi.org/10.1002/aic.10574.

Plummer, L. N., Wigley, T. L. M., and Parkhurst, D. L. 1978. The Kinetics of Calcite Dissolution in CO_2-Water Systems at 5°C to 60°C and 0.0 to 1.0 atm of CO_2. *Am. J. Sci.* **278** (2): 179–216. https://doi.org/10.2475/ajs.278.2.179.

Pluymakers, A., Kobchenko, M., and Renard, F. 2017. How Microfracture Roughness Can Be Used to Distinguish Between Exhumed Cracks and In-Situ Flow Paths in Shales. *J. Struct. Geol.* **94:** 87–97. https://doi.org/10.1016/j.jsg.2016.11.005.

Pokrovsky, O. S., Golubev, S., and Castillo, J. A. 2009. Calcite, Dolomite, and Magnesite Dissolution Kinetics in Aqueous Solutions at Acid to Circumneutral pH, 25 to 150°C and 1 to 55 Atm PCO_2: New Constraints on CO_2 Sequestration in Sedimentary Basins. *Chemical Geology* **265** (1): 20–32. https://doi.org/10.1016/j.chemgeo.2009.01.013.

Ratnakar, R. R., Kalia, N., and Balakotaiah, V. 2013. Modeling, Analysis and Simulation of Wormhole Formation in Carbonate Rocks With In Situ Cross-Linked Acids. *Chem. Eng. Sci.* **90:** 179–199. https://doi.org/10.1016/j.ces.2012.12.019.

Rowan, G. 1959. Theory of Acid Treatment of Limestone Formations. *J. Inst. Pet.* **45** (431): 321.

Ruffet, C., Fery, J. J.., and Onaisi, A. 1998. Acid-Fracturing Treatment: A Surface Topography Analysis of Acid Etched Fractures to Determine Residual Conductivity. *SPE J.* **3** (2): 155–162. SPE-38175-PA. https://doi.org/10.2118/38175-PA.

Salwa, S. 2016. Vein Mineralization Analyses. Internal Report of the ShaleSeq Project. POL-NOR 234198/100/2014. Technical report, Polish Geological Institute.

Saupe, D. 1988. Algorithms for Random Fractals. In *The Science of Fractal Images*, ed. H. Peitgen and D. Saupe, pp. 71–136. New York: Springer.

Smith, M., Sholokhova, Y., Hao, Y. et al. 2013. CO_2-Induced Dissolution of Low-Permeability Carbonates. Part I: Characterization and Experiments. *Adv. Water Resour.* **62** (Part C): 370–387. https://doi.org/10.1016/j.advwatres.2013.09.008.

Starchenko, V., Marra, C. J., and Ladd, A. J. 2016. Three-Dimensional Simulations of Fracture Dissolution. *J. Geophys. Res.: Solid Earth* **121** (9): 6421–6444. https://doi.org/10.1002/2016jB013321.

Szymczak, P. and Ladd, A. J. C. 2006. A Network Model of Channel Competition in Fracture Dissolution. *Geophys. Res. Lett.* **33** (5) L05401. https://doi.org/10.1029/2005GL025334.

Szymczak, P. and Ladd, A. J. C. 2009. Wormhole Formation in Dissolving Fractures. *J. Geophys. Res.* **114** (B6): B06203. https://doi.org/10.1029/2008jB006122.

Szymczak, P. and Ladd, A. J. C. 2011. Instabilities in the Dissolution of a Porous Matrix. *Geophys. Res. Lett.* **38** (7): L07403. https://doi.org/10.1029/2011GL046720.

Szymczak, P. and Ladd, A. J. C. 2012. Reactive Infiltration Instabilities in Rocks. Fracture Dissolution. *J. Fluid Mech.* **702:** 239–264. https://doi.org/10.1017/jfm.2012.174.

Szymczak, P. and Ladd, A. J. C. 2013. Interacting Length Scales in the Reactive-Infiltration Instability. *Geophys. Res. Lett.* **40** (12): 3036–3041. https://doi.org/10.1002/grl.50564.

Tripathi, D. and Pournik, M. 2014. Effect of Acid on Productivity of Fractured Shale Reservoirs. Presented at the Unconventional Resources Technology Conference, Denver, 25–27 August. URTEC-1922960-MS. https://doi.org/10.15530/URTEC-2014-1922960.

Upadhyay, V. K., Szymczak, P., and Ladd, A. J. C. 2015. Initial Conditions or Emergence: What Determines Dissolution Patterns in Rough Fractures? *J. Geophys. Res. Solid Earth* **120** (9): 6102–6121. https://doi.org/10.1002/2015jB012233.

Veberič, D. 2012. Lambert W Function for Applications in Physics. *Comput. Phys. Commun.* **183** (12): 2622–2628. https://doi.org/10.1016/j.cpc.2012.07.008.

Virgo, S., Abe, S., and Urai, J. L. 2013. Extension Fracture Propagation in Rocks With Veins: Insight Into the Crack-Seal Process Using Discrete Element Method Modeling. *J. Geophys. Res. Solid Earth* **118** (10): 5236–5251. https://doi.org/10.1002/2013jB10540.

Walsh, J. B., Brown, S. R., and Durham, W. B. 1997. Effective Media Theory With Spatial Correlation for Flow in a Fracture. *J. Geophys. Res.* **102** (B10): 22587–22594. https://doi.org/10.1029/97jB01895.

Walton, I. and McLennan, J. 2013. The Role of Natural Fractures in Shale Gas Production. In *Effective and Sustainable Hydraulic Fracturing*, ed. A. P. Bunger, J. McLennan, and R. Jeffrey, pp. 327–356. InTech.

Wu, W. and Sharma, M. M. 2015. Acid Fracturing Shales: Effect of Dilute Acid on Properties and Pore Structure of Shale. Presented at the SPE Hydraulic Fracturing Technology Conference, The Woodlands, Texas, 3–5 February. SPE-173390-MS. https://doi.org/10.2118/173390-MS. [Also, in 2017 *SPE Prod & Oper* **32** (1): 51–63. SPE-173390-PA. https://doi.org/10.2118/173390-PA.]

Zhang, X., Jeffrey, R. G., and Thiercelin, M. 2009. Mechanics of Fluid-Driven Fracture Growth in Naturally Fractured Reservoirs With Simple Network Geometries. *J. Geophys. Res. Solid Earth* **114** (B12): B12406. https://doi.org/10.1029/2009.JB006548.

Zhang, Y., Yang, S., and Zhang, S. 2014. Wormhole Propagation Behavior and Its Effect on Acid Leakoff Under In Situ Conditions in Acid Fracturing. *Transp. Porous Med.* **101:** 99–114.

Piotr Szymczak is an associate professor at the Faculty of Physics, University of Warsaw. Research within his group focuses on the intersection between physics and geosciences, with a specific emphasis on the dissolution processes of porous and fractured rock. Szymczak has published more than 70 papers in peer-reviewed journals and has edited two books. He holds a PhD degree from the University of Warsaw.

Kamil Kwiatkowski is a postdoctoral researcher at the Faculty of Physics, University of Warsaw. He specializes in reactive flow modeling, both in the context of porous and fractured media flows and in the context of catalytic reactors (combustion and gasification of coal and biomass). Kwiatkowski has led several research projects and has published more than 20 papers in peer-reviewed journals. He holds a PhD degree in geophysics from the University of Warsaw.

Marek Jarosinski is the head of the Computational Geology Laboratory Department at the Polish Geological Institute. He specializes in structural geology, geodynamics, geomechanics and numerical modeling, and performing geodynamic and tectonic and geophysical analysis for the petroleum industry. Jarosinskí has led several research projects and is the author of 105 scientific publications. He holds a PhD degree in geology from the Polish Geological Institute.

Tomasz Kwiatkowski is a researcher in the CFD Analyses Team at the Division of Nuclear and Environmental Studies of the National Centre for Nuclear Research (Poland). His area of expertise is large-scale flow and transport simulations, particularly simulations of flow and temperature pulsations in rod bundles. Kwiatkowski holds a BSc degree in environmental physics from the University of Warsaw and an MSc degree from the Warsaw University of Technology.

Florian Osselin is a post-doctoral-degree researcher at the University of Calgary. Previously, he worked as a post-doctoral-degree research assistant at the University of Warsaw. Osselin specializes in the physico-chemistry of porous media, particularly, the coupling between geochemical reactions (precipitation, confined crystallization, dissolution) and the mechanical behavior of the porous materials. He holds an engineering degree from ESPCI ParisTech and a PhD degree from Université Paris-Est.